# Explicit finite-difference lattice Boltzmann method for curvilinear coordinates

Zhaoli Guo and T. S. Zhao*
*Department of Mechanical Engineering, The Hong Kong University of Science and Technology, Hong Kong, China*
(Received 18 December 2002; revised manuscript received 18 April 2003; published 26 June 2003)

In this paper a finite-difference-based lattice Boltzmann method for curvilinear coordinates is proposed in order to improve the computational efficiency and numerical stability of a recent method [R. Mei and W. Shyy, J. Comput. Phys. **143**, 426 (1998)] in which the collision term of the Boltzmann Bhatnagar-Gross-Krook equation for discrete velocities is treated implicitly. In the present method, the implicitness of the numerical scheme is removed by introducing a distribution function different from that being used currently. As a result, an explicit finite-difference lattice Boltzmann method for curvilinear coordinates is obtained. The scheme is applied to a two-dimensional Poiseuille flow, an unsteady Couette flow, a lid-driven cavity flow, and a steady flow around a circular cylinder. The numerical results are in good agreement with the results of previous studies. Extensions to other lattice Boltzmann models based on nonuniform meshes are also discussed.

DOI: 10.1103/PhysRevE.67.066709 PACS number(s): 83.85.Pt, 47.11.+j, 02.60.Cb, 02.70.Bf

## I. INTRODUCTION

The last decade has witnessed a rapid development of the lattice Boltzmann method (LBM) as an effective tool for simulating fluid flows and for modeling other complex systems [1–4]. Historically, LBM evolved from the lattice-gas automata (LGA) method. Later it was realized that the lattice Boltzmann equation (LBE) could also be derived from the continuous Boltzmann equation by choosing an appropriate set of discrete velocities [5,6] based on some special discretization schemes. This point of view opens a door for better understanding of the basis of LBM, and provides a solid theoretical foundation for LBM. Following this method, a variety of lattice Boltzmann models for thermal [7], multiphase [8], and multicomponent [9] systems have been proposed, based on different continuous kinetic equations.

The idea that LBE is a discrete scheme of the continuous Boltzmann equation also provides a way to improve the computational efficiency and accuracy of LBM. From this idea, the discretization of the phase space and the configuration space can be done independently [5]. Once the phase space is discretized, any standard numerical technique can serve the purpose of solving the discrete velocity Boltzmann equation (DVBE). It is not surprising that the finite-difference, finite-volume, and finite-element methods have been introduced into LBM in order to increase computational efficiency and accuracy by using nonuniform grids. The first finite-difference LBE (FDLBE) was perhaps due to Reider and Sterling [10], and was examined by Cao *et al.* in more detail [11]. Finite-difference LBM was further extended to curvilinear coordinates with nonuniform grids by Mei and Shyy [12]. The study of FDLBE is still in progress [13–15]. The first attempt to combine the finite-volume method with LBE is attributed to Nannelli and Succi [1,16], who obtained a finite-volume LBE (FVLBE) for the volume-averaged ''coarse-grain'' distribution function starting from the DVBE for the ''fine-grain'' distribution function. Later, some other FVLBE formulations were proposed, based on ''modern'' finite-volume techniques [17–20]. Recently, the finite-element method has also been introduced into LBM [21].

In deriving discrete schemes for the DVBE, the collision term of the DVBE can be treated either explicitly or implicitly. The time marching is trivial for explicit schemes. But if the collision term is treated implicitly, some special considerations should be taken for the sake of computational efficiency and accuracy of the scheme, since the collision operator is usually a nonlinear function of the distribution function. Cao *et al.* [11] proposed to use a second-order Runge-Kutta method for time marching of the FDLBE. Mei and Shyy [12] suggested to use a second extrapolation method to determine the unknown collision term at the new time level in the FDLBE for curvilinear coordinates. Lee and Lin [21] used a predictor-corrector method for the time marching of their finite-element LBE (FELBE) [21]. Nevertheless, to our knowledge, all the existing FVLBEs [16–20] use an explicit form of the collision operator.

In this work, we present an improved version of the FDLBE first proposed by Mei and Shyy [12]. In our model, the collision term is treated implicitly, just as done in the Mei-Shyy model. However, the implicitness of the discrete scheme is completely removed by introducing another distribution function based on the earlier distribution function, and we finally obtain a simple explicit scheme like the standard LBE. Furthermore, this trick for the FDLBE can also be easily used to develop more efficient FVLBE and FELBE schemes.

## II. NUMERICAL FORMULATIONS

### A. Reexamination of Mei and Shyy's FDLBE

The starting point of the FDLBE proposed by Mei and Shyy [12] is the continuous discrete velocity Boltzmann equation

$$\frac{\partial f_i}{\partial t} + \mathbf{e}_i \cdot \nabla f_i = \Omega_i , \tag{1}$$

where $\mathbf{e}_i$ is the discrete particle velocity, $f_i$ is the distribution function (DF) associated with $\mathbf{e}_i$, and $\Omega_i$ is the collision

*Electronic address: metzhao@ust.hk

 

operator. In the kinetic theory, the collision operator is very complicated and is usually approximated by the simple single-relaxation-time Bhatnagar-Gross-Krook (BGK) model in LBM,

$$\Omega_i = -\frac{1}{\tau}(f_i - f_i^{(eq)}), \tag{2}$$

where $\tau$ is the relaxation time and $f_i^{(eq)}$ is the local equilibrium distribution function (EDF). The macroscopic density $\rho$ and velocity $\mathbf{u}$ of the fluid are determined by the following velocity moments of the DF:

$$\rho = \sum f_i, \quad \rho\mathbf{u} = \sum \mathbf{e}_i f_i. \tag{3}$$

The discrete velocities and the EDFs must be chosen appropriately, such that the mass and momentum are conserved and some symmetry requirements are satisfied in order that the resulting macroscopic equations describe the correct hydrodynamics of the fluid. Here we choose the two-dimensional nine-bit [22] model as an example, with the EDF defined as

$$f_i^{(eq)} = \omega_i \rho \left[ 1 + \frac{\mathbf{e}\cdot\mathbf{u}}{c_s^2} + \frac{\mathbf{uu}:(\mathbf{e}_i\mathbf{e}_i - c_s^2\mathbf{I})}{2c_s^4} \right], \tag{4}$$

where the discrete velocities are given by $\mathbf{e}_0 = \mathbf{0}$, and $\mathbf{e}_i = \lambda_i(\cos\theta_i, \sin\theta_i)$ with $\lambda_i = 1$, $\theta_i = (i-1)\pi/2$ for $i = 1-4$ and $\lambda_i = \sqrt{2}$, $\theta_i = (i-5)\pi/2 + \pi/4$ for $i = 5-8$. The weights are given by $\omega_0 = 4/9$, $\omega_i = 1/9$ for $i = 1-4$, $\omega_i = 1/36$ for $i = 5-8$, and $c_s = 1/\sqrt{3}$ is the sound speed of the model. It can be shown that the Navier-Stokes equations can be derived from the DVBE (1) through a Chapman-Enskog expansion procedure in the incompressible limit [23]:

$$\frac{\partial \rho}{\partial t} + \nabla\cdot(\rho\mathbf{u}) = 0, \tag{5a}$$

$$\frac{\partial(\rho\mathbf{u})}{\partial t} + \nabla\cdot(\rho\mathbf{uu}) = -\boldsymbol{\nabla} p + \nabla\cdot[\rho\nu(\boldsymbol{\nabla}\mathbf{u} + \mathbf{u}\boldsymbol{\nabla})], \tag{5b}$$

where $p = c_s^2\rho$ is the pressure and the shear viscosity $\nu$ is given by

$$\nu = c_s^2(\tau - \tfrac{1}{2}). \tag{6}$$

Mei and Shyy [12] obtained a FDLBE by discretizing the DVBE (1) with the BGK collision operator for curvilinear coordinates, where the advection term is discretized by a finite-difference scheme in an explicit form and the collision term is treated implicitly in order to increase the numerical stability for high Reynolds number flows. However, due to the nonlinearity of the collision operator, Mei and Shyy proposed to calculate the EDF $f_i^{(eq)}$ at a new time level $t_{n+1}$ using a linear extrapolation scheme from $f_i^{(eq)}$ at time $t_n$ and $t_{n-1}$;

$$f_i^{(eq),n+1} = 2f_i^{(eq),n} - f_i^{(eq),n-1}. \tag{7}$$

Using this formulation, Mei and Shyy obtained their FDLBE in the form of

$$f_i^{n+1} = f_i^n - \Delta t\,\mathbf{e}_i\cdot\boldsymbol{\nabla}_h f_i^n - \frac{\Delta t}{\tau}[f_i^{n+1} - (2f_i^{(eq),n} - f_i^{(eq),n-1})], \tag{8}$$

where $\boldsymbol{\nabla}_h$ is the discretization form of operator $\boldsymbol{\nabla}$. With the extrapolation treatment of the collision term, the FDLBE (8) can be solved explicitly. However, as pointed out by Mei and Shyy, the extrapolation method is subject to numerical instability.

### B. A new explicit FDLBE

In order to improve the numerical stability, we propose a treatment for the collision term in discretizing the DVBE. To this end, we first integrate the DVBE (1) over a time interval $[t_n, t_{n+1}]$ to get

$$f_i^{n+1} - f_i^n + \Delta t\,\mathbf{e}_i\cdot\boldsymbol{\nabla} f_i^n = \Delta t[\theta\Omega_i^{n+1} + (1-\theta)\Omega_i^n], \tag{9}$$

where $t_{n+1} = t_n + \Delta t$ and $0 \leqslant \theta \leqslant 1$. Note that the advection term is evaluated at $t_n$, just as done in Mei and Shyy's original FDLBE. $\theta = 0$ or 1 means that the collision term is treated, explicitly or implicitly, completely. But to achieve a second-order approximation, one must choose $\theta = 1/2$.

To remove the implicitness of Eq. (9) for an arbitrary $\theta$, we introduce the following distribution function based on $f_i$ and $f_i^{(eq)}$:

$$g_i = f_i + \omega\theta(f_i - f_i^{(eq)}), \tag{10}$$

where $\omega = \Delta t/\tau$. By applying this DF to Eq. (9), we obtain the following semidiscretized Boltzmann equation:

$$g_i^{n+1} + \frac{\Delta t}{1+\omega\theta}\mathbf{e}_i\cdot\boldsymbol{\nabla}(g_i^n + \omega\theta f_i^{(eq),n}) = \frac{1-\omega(1-\theta)}{1+\omega\theta}(g_i^n + \omega\theta f_i^{(eq),n}) + \omega(1-\theta)f_i^{(eq),n} \tag{11}$$

or

$$g_i^{n+1} + \Delta t\,\mathbf{e}_i\cdot\boldsymbol{\nabla} f_i^n = (1-\omega+\omega\theta)f_i^n + \omega(1-\theta)f_i^{(eq),n}, \tag{12}$$

where

$$f_i^n = \frac{1}{1+\omega\theta}(g_i^n + \omega\theta f_i^{(eq),n}). \tag{13}$$

Once the gradient operator is discretized, the DF $g_i$ can evolve according to Eq. (12), given that $g_i$ (or $f_i$) is initialized. The macroscopic density and velocity of the fluid can be determined from the DF $g_i$ directly. In fact, from Eq. (10) we can obtain

$$\rho = \sum g_i, \quad \rho\mathbf{u} = \sum \mathbf{e}_i g_i. \tag{14}$$

It is noted that a similar procedure has been used by He *et al*. in order to remove the implicitness of the collision term [7]. But surprisingly, this technique has never been employed by other authors in designing FD-, FV-, or FE-based LBEs. In fact, it is quite easy to utilize this trick to improve the performance of these coupled LBEs. For example, in the FELBE proposed by Lee and Lin [21], the evolution equation reads

$$f_i^{n+1} = -\omega(f_i^{n+1/2} - f_i^{(eq),n+1/2}) + R_i^n, \tag{15}$$

where $R_i^n$ is the collective of terms containing only $f_i^n$ and $f_i^{(eq),n}$. In order to approximate $f_i^{(eq),n+1/2}$, Lee and Lin proposed a predictor-corrector method. However, if we approximate $f_i^{n+1/2}$ and $f_i^{(eq),n+1/2}$ by the Crank-Nicolson method, i.e., $f_i^{n+1/2}=(f_i^{n+1}+f_i^n)/2$ and $f_i^{(eq),n+1/2}=(f_i^{(eq),n+1}+f_i^{(eq),n})/2$, and use the EDF $g_i$ with $\theta=1/2$, we can finally obtain an explicit FELBE with, in principle, at least the same numerical stability and accuracy as the original one.

We now discuss the discretization of the spatial gradient operator $\boldsymbol{\nabla}$ for a general curvilinear coordinate $\boldsymbol{\xi}$. For such a coordinate, the advection term in Eq. (1) can be written as

$$\mathbf{e}_i \cdot \boldsymbol{\nabla} f_i = e_{i\alpha}\frac{\partial f_i}{\partial x_\alpha} = c_{i\beta}\frac{\partial f_i}{\partial \xi_\beta}, \tag{16}$$

where $c_{i\beta}=e_{i\alpha}\partial\xi_\beta/\partial x_\alpha$. The central difference of $\partial f_i/\partial\xi_\beta$ takes the form of

$$\frac{\partial f_i}{\partial \xi_\beta}\Big|_c = \frac{1}{2\Delta\xi_\beta}[f_i(\xi_\beta+\Delta\xi_\beta,\cdot) - f_i(\xi_\beta-\Delta\xi_\beta,\cdot)], \tag{17}$$

where $\Delta\xi_\beta$ is the mesh spacing in the $\xi_\beta$ direction. It is well known that the central difference is less dissipative and is easy to implement. However, it is less stable and may produce undesirable oscillations in the solution. An alternative scheme is the following second-order upwind-difference scheme:

$$\frac{\partial f_i}{\partial \xi_\beta}\Big|_u = \begin{cases} \dfrac{1}{2\Delta\xi_\beta}[3f_i(\xi_\beta,\cdot) - 4f_i(\xi_\beta-\Delta\xi_\beta,\cdot) + f_i(\xi_\beta-2\Delta\xi_\beta,\cdot)] & \text{if} \quad c_{i\beta}\geqslant 0 \\ -\dfrac{1}{2\Delta\xi_\beta}[3f_i(\xi_\beta,\cdot) - 4f_i(\xi_\beta+\Delta\xi_\beta,\cdot) + f_i(\xi_\beta+2\Delta\xi_\beta,\cdot)] & \text{if} \quad c_{i\beta}<0. \end{cases} \tag{18}$$

Usually, the second-order upwind scheme is more stable than the central-difference scheme. However, strong numerical dissipation may appear in simulations, especially for flows with high Reynolds numbers. An approach to solve this problem is to combine the upwind scheme with the central scheme to form a mixed-difference scheme

$$\frac{\partial f_i}{\partial \xi_\beta}\Big|_m = \epsilon\frac{\partial f_i}{\partial \xi_\beta}\Big|_u + (1-\epsilon)\frac{\partial f_i}{\partial \xi_\beta}\Big|_c, \tag{19}$$

where $0\leqslant\epsilon\leqslant 1$ is a control parameter to adjust the weight of the central and upwind schemes. It is noted that Mei and Shyy have proposed another approach for mixing the central and upwind schemes [12]. That is, the advection term in each direction is separately approximated with the central and upwind schemes. The mixed scheme seems to be able to produce satisfactory results.

By applying the mixed finite-difference scheme given by Eq. (19) to the semidiscretized DVBE (12), we finally obtain a finite-difference-based LBE in the form of

$$g_i^{n+1} + \Delta t\,\mathbf{e}_i\cdot\boldsymbol{\nabla}_h f_i^n = (1-\omega+\omega\theta)f_i^n + \omega(1-\theta)f_i^{(eq),n}, \tag{20}$$

where $\boldsymbol{\nabla}_h$ is the mixed-difference scheme defined by Eq. (19). With appropriate initial and boundary conditions (see below), the present FDLBE is implemented in the following three steps at each time step:

(1) Given $g_i^n$, compute $\rho^n$, $\mathbf{u}^n$, and $f_i^{(eq),n}$ first, and then $f_i^n$ according to Eq. (13).

(2) Compute the finite difference of $f_i^n$ according to Eq. (19).

(3) Compute $g_i^{n+1}$ according to Eq. (20).

It is noted that if $\theta$ is set to be 1, the present FDLBE is identical with the scheme proposed by Mei and Shyy [12] in essence, but the formulation of the present FDLBE is more concise. More importantly, the implicitness of the EDF does not appear explicitly in the present scheme, such that no special treatments (such as extrapolation or predictor corrector) are needed and therefore, the numerical stability and accuracy depend only on the scheme itself.

### C. Initial and boundary conditions

Initial and boundary conditions are usually given in terms of macroscopic physical variables such as $\rho$ and $\mathbf{u}$. But in LBM, the initial and boundary conditions should be implemented through the distribution function $f_i$. How to determine the initial and boundary values of the DF is an important issue in LBM.

In many applications, the DF is initialized to be equal to the EDF, i.e., $f_i(\mathbf{x},t_0)=f_i^{(eq)}(\mathbf{x},t_0)$. This approach works well for steady flows. A more elaborate approach, which involves the spatial gradient of velocity, was proposed by Skordos [24]. The basic idea of Skordos' approach is to include

the nonequilibrium part in initializing the DF. Specifically, the DF is initialized to be

$$f_i = f_i^{(eq)} + f_i^{(1)}, \tag{21}$$

where $f_i^{(1)}$ is the simplified nonequilibrium part of the DF by neglecting the second-order terms in the Mach number Ma:

$$f_i^{(1)} = -\tau\omega_i \left[ \frac{1}{c_s^2} \mathbf{e}_i \mathbf{e}_i : \nabla(\rho \mathbf{u}) - \nabla \cdot (\rho \mathbf{u}) \right]. \tag{22}$$

In fact, by noticing that density fluctuation $\delta\rho$ is of second order in Ma [$\delta\rho = O(\mathrm{Ma}^2)$] in the incompressible limit, we can further simplify the expression of the nonequilibrium DF (22) to

$$f_i^{(1s)} = -\frac{\rho_0 \tau \omega_i}{c_s^2} \mathbf{e}_i \mathbf{e}_i : \nabla \mathbf{u}, \tag{23}$$

where $\rho_0$ is the average density.

Treatment of boundary conditions also plays an important role in LBM since it influences both accuracy and stability of the computation. Mei and Shyy proposed a method [12] for their FDLBE, based on the extrapolation method proposed by Chen *et al.* [25], and a similar idea was adopted by Lee and Lin for their FELBE [21]. The extrapolation method can preserve the overall accuracy of LBE, and can be applied to a variety of boundary conditions. Unfortunately, the numerical stability of this extrapolation method is rather poor [26,27] for high Reynolds number flows. Recently, a method based on the extrapolation of the nonequilibrium DF was proposed by Guo *et al.* for flat or curved boundaries [27,28]. The nonequilibrium extrapolation method is similar to the original extrapolation method, but the former is more stable than the latter. The nonequilibrium extrapolation method can be easily extend for LBE in curvilinear coordinates. Assume that $\mathbf{x}_b$ is a boundary node, and that $\mathbf{x}_f$ is the nearest neighboring fluid node of $\mathbf{x}_b$ (for instance, $\mathbf{x}_f = \mathbf{x}_b + \mathbf{e}_i \Delta x$ in a uniform lattice). Then, the DF at $\mathbf{x}_b$ is set to be

$$f_i(\mathbf{x}_b) = f_i^{(eq)}(\mathbf{x}_b) + [f_i(\mathbf{x}_f) - f_i^{(eq)}(\mathbf{x}_f)], \tag{24}$$

where the second part in the brackets on the right-hand side is the nonequilibrium part of the DF at $\mathbf{x}_f$, which is used to approximate that at node $\mathbf{x}_b$.

Finally, based on Eqs. (10), (23), and (24) the DF $g_i$ can be initialized as

$$g_i(\mathbf{x}, t_0) = f_i^{(eq)}(\mathbf{x}, t_0) - \frac{\rho_0 \theta \Delta t \omega_i}{c_s^2} \mathbf{e}_i \mathbf{e}_i : \nabla \mathbf{u}(\mathbf{x}, t_0) \tag{25}$$

and the DF at a boundary node is set to be

$$g_i(\mathbf{x}_b, t) = f_i^{(eq)}(\mathbf{x}_b, t) + [g_i(\mathbf{x}_f, t) - f_i^{(eq)}(\mathbf{x}_f, t)]. \tag{26}$$

The boundary conditions, such as velocity $\mathbf{u}(\mathbf{x}_b)$, are imposed on the EDF $f_i^{(eq)}$. It is noted that the present treatment of the boundary conditions is different from those used in Refs. [12] and [21] both of which solve the FDLBE (20) on the boundary nodes.

### D. Analysis of the FDLBE

In this section we analyze the numerical accuracy and stability of the present FDLBE (20). Since this scheme is identical with scheme (9) if the gradient operator $\nabla$ in Eq. (9) is replaced by the discretized version $\nabla_h$, both the schemes exhibit the same numerical stability and accuracy. Therefore, we choose scheme (9) to discuss its stability and accuracy. Obviously, the temporal accuracy for the transient and collision terms is of second order if we take $\theta = 0.5$, but is only of first order for the convection term. Therefore, the overall temporal accuracy of the scheme is of first order. The spatial accuracy depends on the discrete gradient operator $\nabla_h$ which is obviously of second order for the three (central, second-order upwind, and mixed) schemes considered in this work. It should be emphasized that the temporal and spatial accuracy of the present FDLBE is for the DVBE (1), not for the incompressible Navier-Stokes equations. In fact, there exists an additional error (compressible error) as applied the FDLBE to the incompressible Navier-Stokes equations. The compressible error is of order $O(\mathrm{Ma}^2)$, where Ma is the Mach number of the flow. Convergence solution to the incompressible Navier-Stokes equations for a fixed Reynolds number can be obtained only as $\Delta t$, $\Delta x$, and Ma are all small enough.

The numerical stability of the FDLBE is studied via the von Neumann linearized stability analysis proposed by Sterling and Chen [23]. For simplicity, in what follows, we assume that $\nabla_h$ is discretized on a uniform mesh with a spacing $\Delta x$. We first expand $f_i(\mathbf{x}, t)$ as

$$f_i(x, t) = \overline{f_i^{(eq)}(\mathbf{x}, t)} + f_i'(\mathbf{x}, t), \tag{27}$$

where $\overline{f_i^{(eq)}(\mathbf{x}, t)}$ is the global EDF, which is a constant that does not vary in space or time but depends on the mean density $\overline{\rho}$ and velocity $\overline{\mathbf{u}}$. $f_i'(\mathbf{x}, t)$ is the fluctuation of $f_i$ that is not necessarily equal to $f_i^{(neq)}$. With this expansion, Eq. (9) can be rewritten as

$$[\delta_{ij} - \theta \Delta t E_{ij}] f_j'(\mathbf{x}, t + \Delta t) = [\delta_{ij} + (1 - \theta) \Delta t E_{ij}] f_j'(\mathbf{x}, t) - \Delta t \mathbf{e}_i \cdot \nabla_h f_i'(\mathbf{x}, t), \tag{28}$$

where $E_{ij} \equiv \partial \Omega_i [\overline{f_i^{(eq)}(\mathbf{x}, t)}] / \partial f_j$ is the Jacobian matrix of the collision operator and does not depend on time and location.

By taking the Fourier transform of Eq. (28), we obtain

$$F_i(\mathbf{k}, t + \Delta t) = G_{ij} F_j(\mathbf{k}, t), \tag{29}$$

where $F_j(\mathbf{k}, t) = \int f_j'(\mathbf{x}, t) \exp(-i\mathbf{k} \cdot \mathbf{x}) d\mathbf{x}$ and $\mathbf{k} = (k_x, k_y)$ is the wave number. Matrix $\mathbf{G}$ is given by

$$\mathbf{G} = (\mathbf{I} - \Delta t \theta \mathbf{E})^{-1} [\mathbf{I} + (1 - \theta) \Delta t \mathbf{E} - r\mathbf{S}], \tag{30}$$

where $\mathbf{I}$ is the $9 \times 9$ identity matrix, $r = \Delta t \Delta x$ is the ratio between the time step and the mesh spacing, and $\mathbf{S}$

$=\mathrm{diag}(s_0,\ldots,s_8)$ depends on the discrete gradient operator. For the mixed scheme (19) on the uniform mesh,

$$s_j = i(1-\epsilon)(\sin\vartheta_{jx}+\sin\vartheta_{jy}) + \frac{\epsilon}{2}[6-4\exp(-i\vartheta_{jx}) - 4\exp(-i\vartheta_{jy})+\exp(-i2\vartheta_{jx})+\exp(-2i\vartheta_{jy})], \tag{31}$$

where $\vartheta_{jx}=k_x e_{jx}\Delta x$ and $\vartheta_{jy}=k_y e_{jy}\Delta x$.

The stability of the present scheme depends on the eigenvalues of matrix **G**. If the wave number **k** is zero, the diagonal matrix **S** becomes zero, and the eigenvalues of **G** are determined by those of matrix **E**. Obviously, the elements of matrix **E** are functions of the mean velocity $\overline{\mathbf{u}}$. But it is interesting to recognize that its eigenvalues are unrelated to $\overline{\mathbf{u}}$ and depend only on the relaxation time $\tau$. In fact, the eigenvalues of matrix **E** are 0 and $-1/\tau$, with three and six multiplicities, respectively. Therefore, in this case the eigenvalues of matrix **G** are $\{1,[1-(1-\theta)\omega]/[1+\theta\omega]\}$, where $\omega=\Delta t/\tau$ is the nondimensional collision frequency. Thus, asymptotical stability of the scheme for uniform flows is guaranteed when $\tau>\max\{0,(0.5-\theta)\Delta t\}$.

For general cases, where $\mathbf{k}\neq\mathbf{0}$, the modulus of matrix **G** depends on a number of parameters: the mean velocity $\overline{\mathbf{u}}$, the normalized wave number $\overline{\mathbf{k}}=\mathbf{k}\Delta x$, the nondimensional collision frequency $\omega=\tau/\Delta t$, ratio $r$, and parameters $\theta$ and $\epsilon$. It is difficult to obtain the eigenvalues of **G** analytically, but we can calculate them numerically. Even so, it is still very difficult to assess the complete effects of these parameters on stability. Here we restrict ourselves to the nondimension collision frequency $\omega$ and ratio $r$, with $0\leqslant\overline{\mathbf{k}}\leqslant\pi$ and other parameters fixed.

As pointed by Sterling and Chen [23], for the standard LBE, the most unstable eigenvalue usually occurred when the angle between the mean velocity and the wave number was zero. For this reason, we will also address this case only, and further assume that the mean velocity and the wave number are both aligned with $\mathbf{e}_1$. In Fig. 1, the stability region is shown as a function of $\omega$ and $r$, for different values of $\epsilon$, with $|\overline{\mathbf{u}}|=0.1$ and $\theta=0.5$. It is observed that for the central-difference scheme, a stability region still exists, which is different from the case for a pure wave equation. This indicates that the collision term can enhance the stability of the scheme. It is also observed that the stability region increases with $r$ until it reaches an upper limit $r_c(<1)$, which depends on the mean velocity $\overline{\mathbf{u}}$. As $r>r_c$, the stability region does not increase with $r$. That is to say, the second-order upwind-difference scheme is not the most stable scheme for the present FDLBE. These observations demonstrate the complicated dependence of the stability of the FDLBE on the parameters.

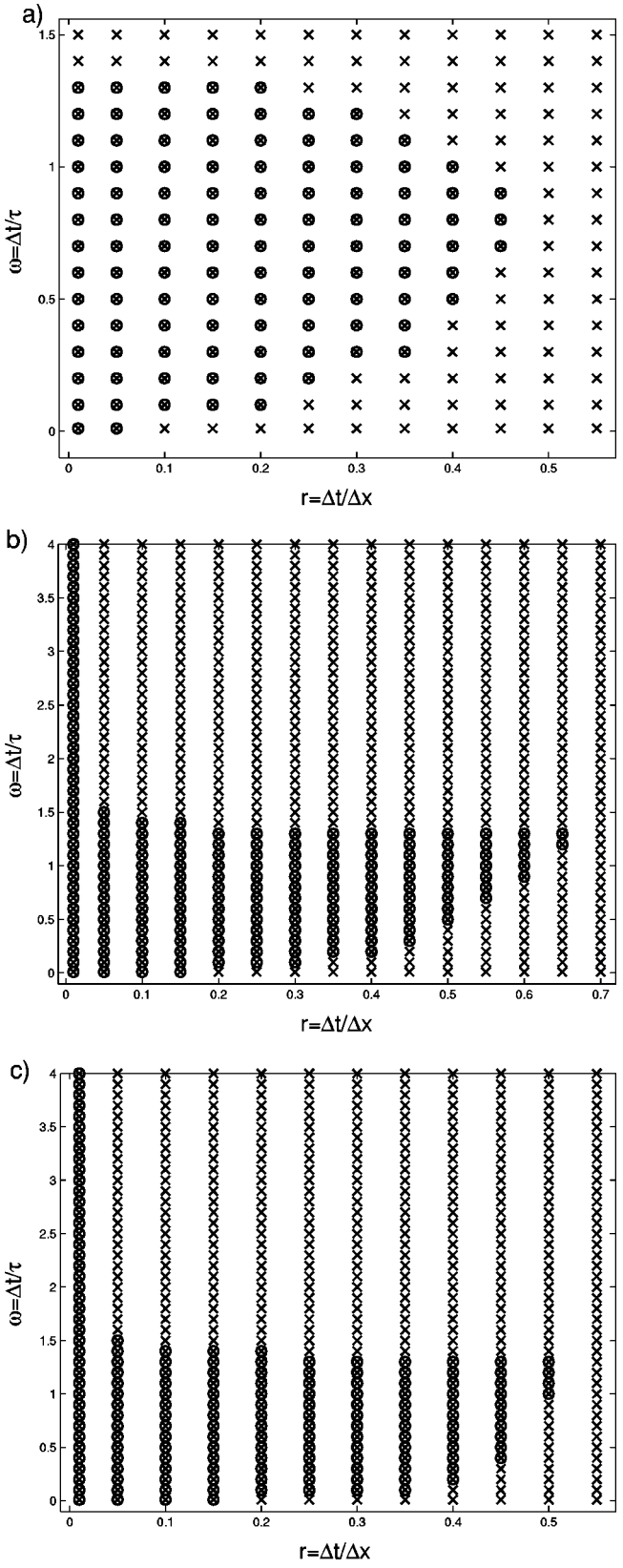


FIG. 1. Stable and unstable regions of the present FDLBE with $|\overline{\mathbf{u}}|=0.1$ and $\theta=0.5$. $\times$, unstable; $\otimes$, stable. (a) the second-order central scheme; (b) the mixed scheme with $\epsilon=0.5$; and (c) the second-order upwind scheme.

## III. NUMERICAL RESULTS

To validate the present FDLBE outlined above, we have applied it to several two-dimensional steady and unsteady flows, including the Poiseuille flow, the Taylor vortex flow, the Couette flow, the cavity flow, and the flow around a cir-

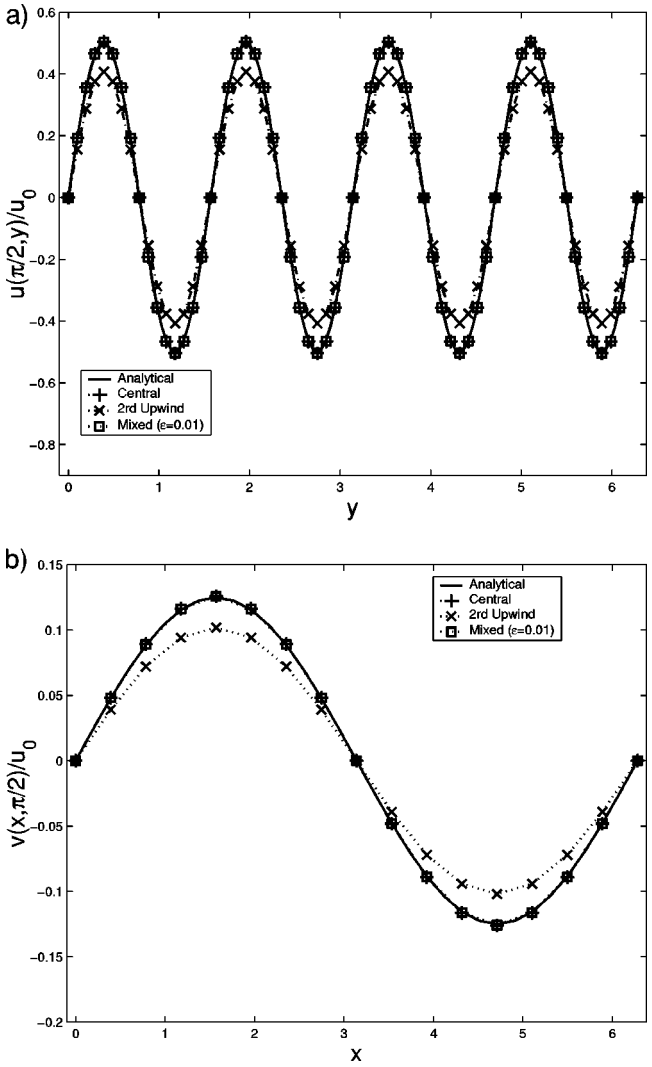


FIG. 2. Velocity profiles of the Taylor vortex flow through the domain center. (a) $u$ component along the vertical line and (b) $v$ component along the horizontal line.

cular cylinder. Quantitative comparisons between the FDLBE results and previous analytical and numerical results are also presented. We choose $\theta=1/2$ for all cases.

### A. The Taylor vortex flow

We first use the Taylor vortex flow to test the accuracy and stability of the present FDLBE for different spatial discretizations. The Taylor vortex flow in a square box has the following analytical solution:

$$u=-u_0\cos(k_1x)\sin(k_2y)\exp[-\nu(k_1^2+k_2^2)t],$$

$$v=u_0\frac{k_1}{k_2}\sin(k_1x)\cos(k_2y)\exp[-\nu(k_1^2+k_2^2)t], \quad (32)$$

$$p=p_0-\frac{u_0^2}{4}\left[\cos(2k_1x)+\frac{k_1^2}{k_2^2}\cos(2k_2y)\right]\times\exp[-2\nu(k_1^2+k_2^2)t],$$

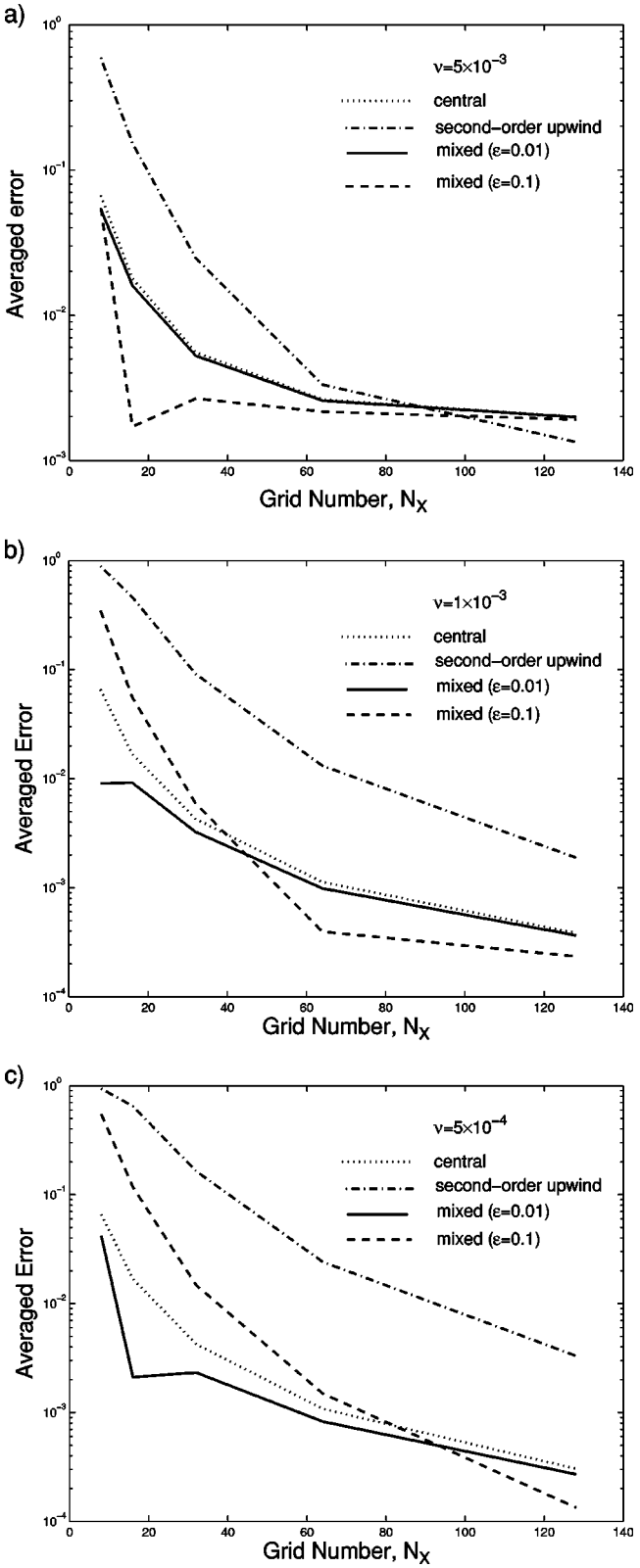


FIG. 3. Averaged errors in the velocity field of the Taylor vortex flow. (a) $\nu=5\times10^{-3}$; (b) $\nu=1\times10^{-3}$; and (c) $\nu=5\times10^{-4}$.

where $p_0$ is the average pressure. In our simulations, the flow is confined to domain $-\pi\leqslant x,y\leqslant\pi$, which is covered by a mesh of size $Nx\times Ny=32\times128$. The wave numbers are set to be $k_1=1.0$ and $k_2=4.0$ and $u_0$ is chosen to be $u_0=0.01$ so

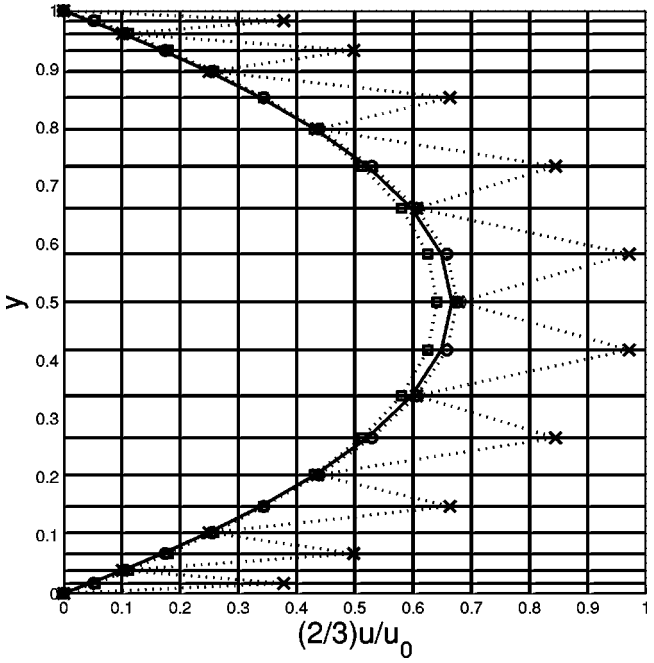


FIG. 4. Mesh distribution and velocity profiles of the Poiseuille flow. Solid line, analytical solution; *o*, central scheme; □, second-order upwind scheme; and ×, mixed scheme with $\epsilon=0.1$.

that the compressibility of the fluid is negligible. The shear viscosity $\nu$ is set to be 0.001 and the time step is set to be $\pi/640$. The flow is initialized by evaluating the analytical solution at $t=0$. The density is initialized based on the equation of state as $\rho=\rho_0+\delta p/c_s^2$, where $\rho_0=p_0/c_s^2$ is set to be unity and pressure fluctuation $\delta p=p-p_0$ is evaluated from Eq. (32). With the velocity and density specified, the DF $g_i$ is then initialized according to Eq. (25). The periodic boundary condition is applied to both directions in all simulations.

The present FDLBE is applied to this Taylor vortex flow using different spatial discretizations. The numerical results for the central, second-order upwind, and mixed schemes ($\epsilon=0.01$) at $t=t_c$ and $t=2t_c$ are plotted in Fig. 2, together with the analytical solutions, where $t_c=\ln 2/[\nu(k_1^2+k_2^2)]$ is the time at which the amplitude of the vortex is halved. One can see that the results of the FDLBE using the central- or mixed-difference scheme agrees well with the analytical solutions. However, the results using the second-order upwind scheme deviate the analytical solutions significantly, which demonstrates the severe numerical dissipative nature of the upwind scheme although it is of second-order accuracy. The central finite-difference scheme can produce reasonable results, as long as the computation is stable. The mixed scheme, which includes the upwind effect slightly, can improve the stability of the computation, and the results appear to be a little more accurate than the pure central scheme. For example, the relative errors for velocity components $u$ and $v$ are $e_c(u)=0.894\%$, $e_c(v)=0.884\%$ and $e_m(u)=0.678\%$, $e_m(v)=0.666\%$ for the central and mixed schemes, respectively.

To further demonstrate this point, we conducted a number of simulations for the Taylor vortex flow with different viscosities using the present FDLBE on different meshes. The

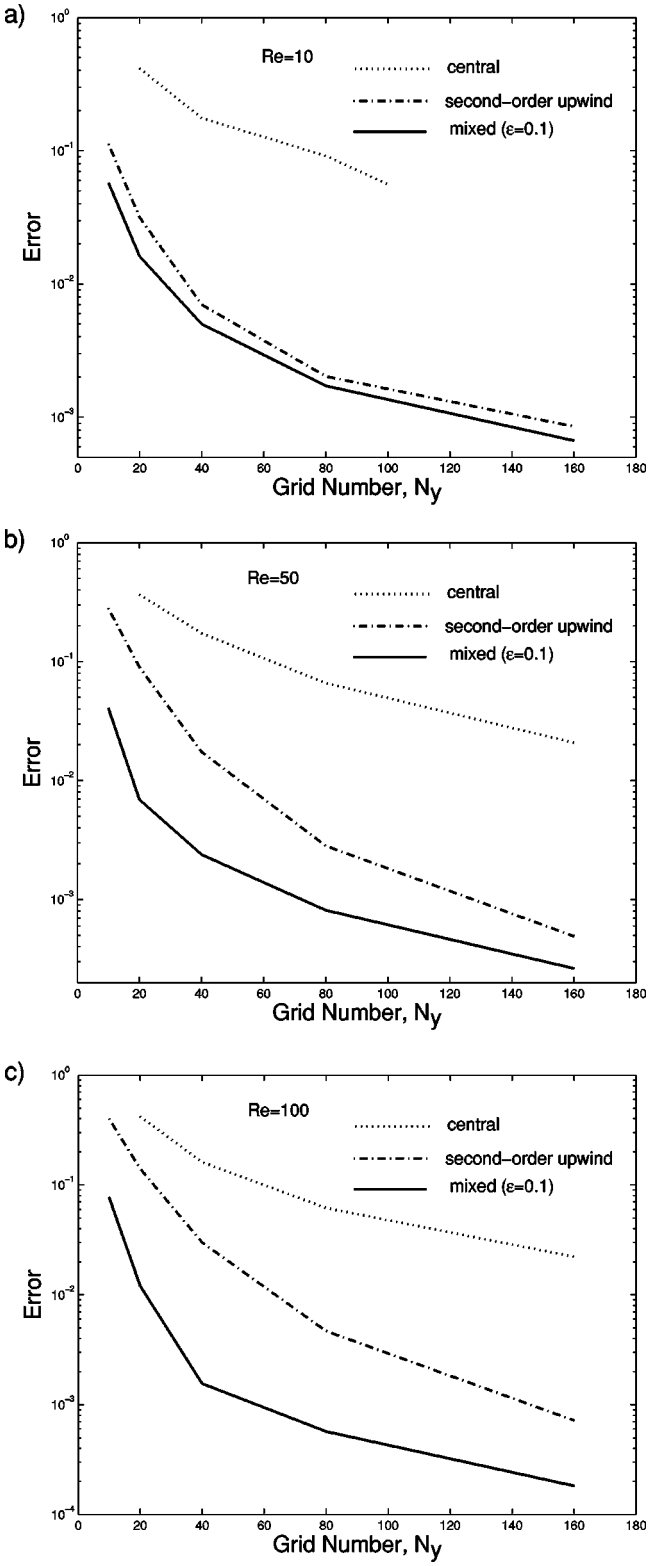


FIG. 5. Errors in the velocity field of the Poiseuille flow. (a) Re=10; (b) Re=50; and (c) Re=100.

errors between the numerical solutions and the analytical solutions are measured at each time step, up to $t_c$. The averaged errors are plotted in Fig. 3 as a function of the number of grid in the *x* direction and the viscosity. It is observed that

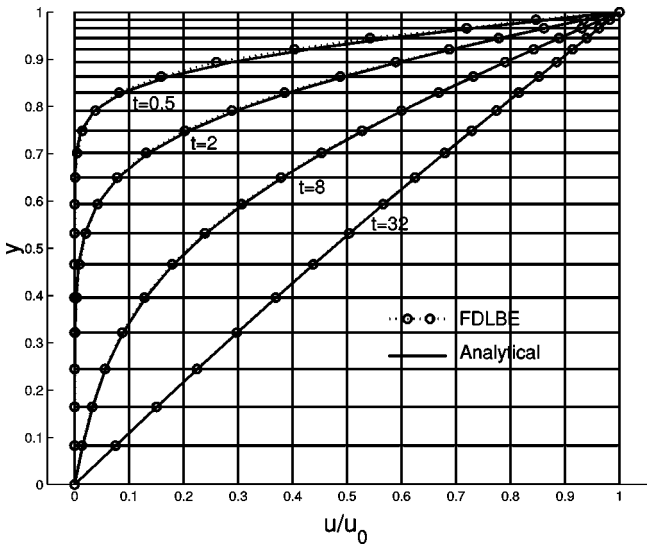


FIG. 6. Mesh distribution and velocity profiles at different times of the unsteady Couette flow.

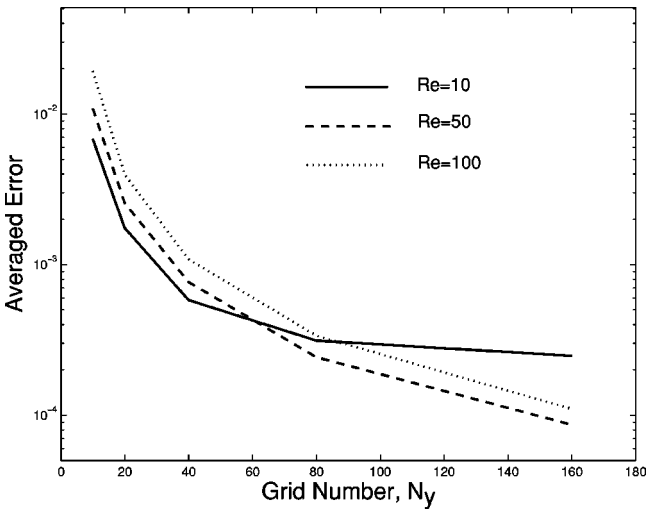


FIG. 7. Averaged errors in the velocity field of the Couette flow.

the upwind scheme produces relatively larger errors compared with other three schemes, especially at small resolutions. The mixed scheme usually yields improved results as the resolution increases. We also observed that the central scheme and the mixed scheme with $\epsilon=0.01$ demonstrate a second-order convergence rate in space, but the other two schemes including the upwind effect have a faster convergence rate. It is also seen that the errors reduce with a slower rate as the mesh is fine enough. This is because the compressible and temporal errors become predominant in these cases. As the viscosity decreases to $1\times10^{-4}$, it is found that the central scheme and the mixed scheme, with $\epsilon=0.01$, become unstable but the other two schemes are still stable and can produce reasonable results with fine enough grids. These facts indicate the potential of the mixed scheme in simulating flows with high Reynolds numbers.

### B. The Poiseuille flow

The Poiseuille flow is a channel flow driven by a constant force between two parallel plates. Under steady state, the velocity profile is expressed as a parabola centered around the axis of the channel;

$$u_x(y)=4u_0\frac{y}{H}\left(1-\frac{y}{H}\right) \quad \text{for} \quad 0\leqslant y\leqslant H, \tag{33}$$

where $H$ is the channel height, $u_0=FH^2/(8\rho_0\nu)$ is the peak velocity, and $F$ is the driven force. The Reynolds number of the Poiseuille flow is based on the peak velocity and the channel height $\mathrm{Re}=Hu_0/\nu$. The driving force $F$ is included in the FDLBE by adding an additional term to Eq. (20).

$$g_i^{n+1}+\Delta t\mathbf{e}_i\cdot\boldsymbol{\nabla}_h f_i^n=(1-\omega+\omega\theta)f_i^n+\omega(1-\theta)f_i^{(eq),n}+\omega_i F\mathbf{e}_{ix}/c_s^2. \tag{34}$$

When applying the present FDLBE to the Poiseuille flow, the nonequilibrium extrapolation scheme (26) is applied to the top and bottom walls of the channel for no-slip boundary conditions, and the periodic boundary condition is applied to both inlet and exit of the channel. The density and velocity of the fluid is initialized to be $\rho=1.0$ and $u=v=0.0$ for the whole domain and the equilibrium method is used to initialize the DF. In simulations, we set $\mathrm{Re}=10.0$ and $L=H=1.0$, where $L$ is the channel length. A nonuniform mesh generated by the following transformation is used:

$$x=\xi,\quad y=\frac{1}{2a}[a+\tanh(c\,\eta)], \tag{35}$$

where $a=\tanh(c)$ and $c>0$ is a parameter controlling the distribution of the mesh. The grid points in the $(\xi,\eta)$ plane are specified by $\xi_i=i/N_x$ and $\eta_j=(2j-N_y)/N_y$ for $i=0,1,\ldots,N_x$ and $j=0,1,\ldots,N_y$. In simulations, the mesh is specified by setting $c=1.5$ and $N_x\times N_y=10\times20$. The mesh distribution is shown in Fig. 4. In all runs, the time step is chosen to be $\Delta t=0.1\times y_1$, where $y_1$ is the distance between the first fluid layer and the bottom plate. The driven force is set to be 0.01 so that the peak velocity $u_0$ is small.

The numerical results for the central-, second-order upwind, and mixed-difference schemes are shown in Fig. 4, together with the analytical solution. One can observe artificial wiggles in the central-difference based solution and numerical dissipation in the second-order upwind-difference based solution. The mixed-difference scheme ($\epsilon=0.1$) again demonstrates good stability and accuracy.

Numerical simulations of the Poiseuille flow at $\mathrm{Re}=50$ and 100 were also conducted on meshes of different size. In Fig. 5, we plotted the numerical errors of the central, second-order upwind, and the mixed schemes as a function of the minimum grid spacing in the $y$ direction. Artificial wiggles were still observed in the numerical solutions of the central scheme, which lead to relatively larger errors compared with the analytical solutions. In fact, the central scheme becomes unstable in the cases of $N_y=10$ and 160 at $\mathrm{Re}=10$. Numerical dissipations also appeared in the second-order upwind-difference based solutions. On the other hand, the mixed-difference scheme ($\epsilon=0.1$) again demonstrates its good

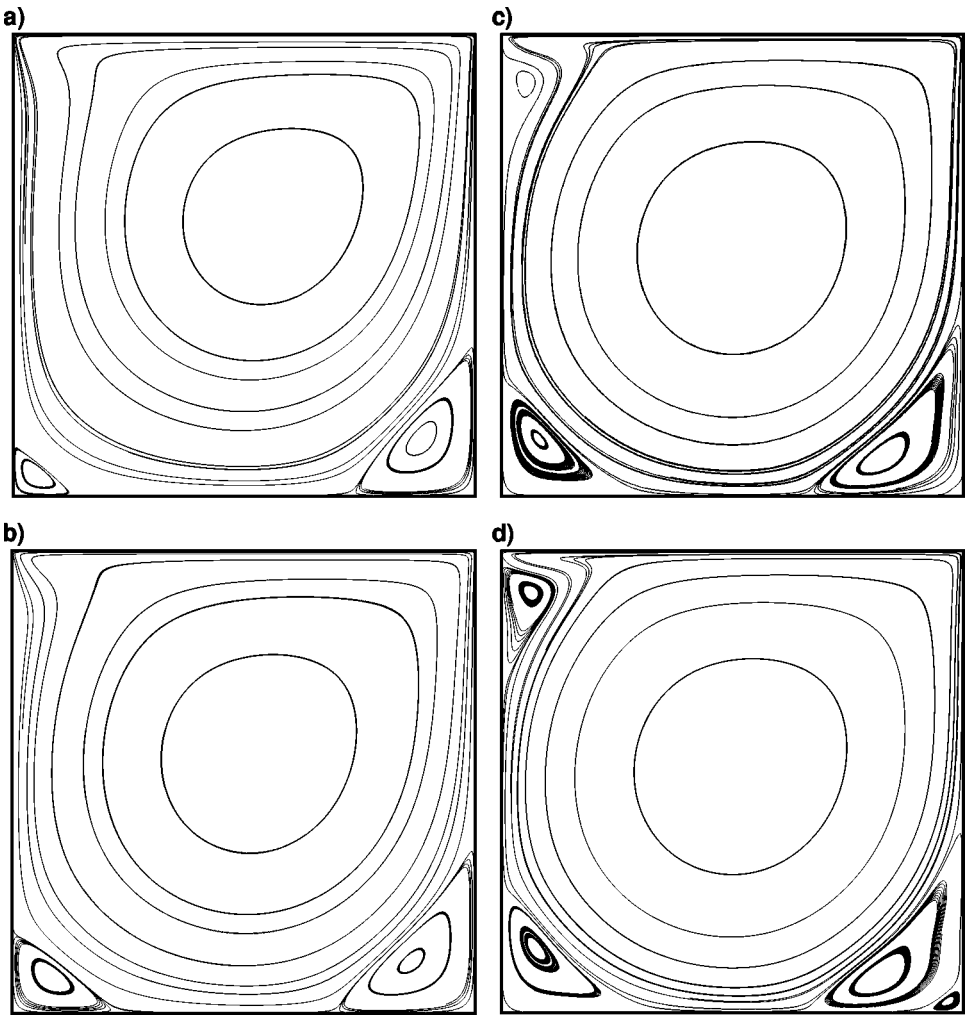


FIG. 8. Streamlines of the cavity flow at different Reynolds numbers. (a) Re=400; (b) Re =1000; (c) Re=3200; and (d) Re=5000.

stability and accuracy. It is also observed that the convergence rate in space of the mixed scheme is similar to that of the central scheme, which is about 2.0 for the Reynolds numbers considered here.

### C. The unsteady Couette flow

The configuration of the unsteady Couette flow is similar to that of the Poiseuille flow, but now the flow is driven by the top plate moving with a constant velocity $u_0$ along the $x$ direction instead of a constant force, and the bottom plate is still kept stationary. The Reynolds number of this flow is defined as $\mathrm{Re}=Hu_0/\nu$, where $H$ is channel height. Initially, the velocity is set to be zero in the whole field. The analytical solution of this flow is expressed as

$$\frac{u(y,t)}{u_0}=\frac{y}{H}+2\sum_{m=1}^{\infty}\frac{(-1)^m}{\lambda_m H}\exp(-\nu\lambda_m^2 t)\sin(\lambda_m y), \tag{36}$$

where $\lambda_m=m\pi/H$, $m=1,2,\ldots$.

In simulations, we set $H=L=1.0$, $u_0=0.1$, and $\mathrm{Re}=10$. A nonuniform mesh of size $N_x\times N_y=10\times 20$, generated by the following transformation is used:

$$x_i=\xi_i,\quad y_j=\frac{\tanh(c\,\eta_j)}{\tanh c}, \tag{37}$$

where $c=1.5$ and $\xi_i=i/N_x$, $\eta_j=j/N_y$ for $i=0-N_x$, $j=0-N_y$. The mesh distribution can be seen in Fig. 6.

The nonequilibrium extrapolation scheme equation (26) is applied to the top and bottom plates, and the periodic boundary condition is applied in the $x$ direction. The FDLBE using the mixed scheme with $\epsilon=0.1$ is applied to this Couette flow. The time step is set to be 0.0016. A series of velocity profiles at different times are shown in Fig. 6 together with the analytical solutions. One can see that the numerical results are in excellent agreement with the analytical solutions. Numerical simulations of this unsteady Couette flow with different Reynolds numbers were also carried out. The time-averaged errors from $t=16$ to 32 were plotted in Fig. 7 against the number of grids in the $y$ direction. Second-order accuracy in space is seen in Fig. 7, and a slower reducing rate in errors is again seen at high resolutions.

### D. Lid-driven cavity flow

The lid-driven cavity flow has been used as a benchmark problem for many numerical methods due to its simple ge-

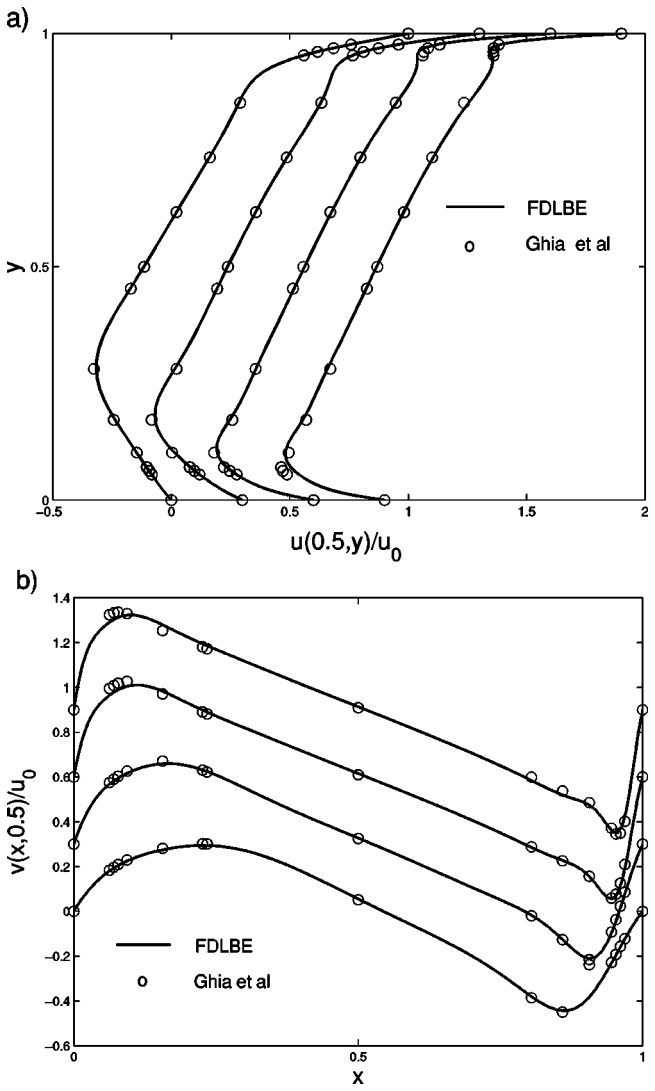


FIG. 9. Velocity profiles of the cavity flow at different Reynolds numbers through the geometric center. (a) $u$ component, from left to right: Re=400, 1000, 3000, 5000 and (b) $v$ component, from bottom to top: Re=400, 1000, 3000, 5000. Note that the profiles are shifted for eyes.

ometry and complicated flow behaviors. It is usually very difficult to capture the flow phenomena near the singular points at the corners of the cavity. Consequently, it is desirable to refine the mesh near these corners.

In this subsection we will apply the present FDLBE to this lid-driven cavity flow in a square cavity of height $H$. The top plate moves from left to right along the $x$ direction with a constant velocity $u_0$, and the other three walls are fixed. The nonequilibrium extrapolation scheme (26) is applied to the four walls, and the equilibrium method is used to initialize the DF by setting $\rho=1.0$ and $\mathbf{u}=0$ in the cavity.

In simulations, the Reynolds number $\mathrm{Re}=Hu_0/\nu$ is chosen to be 400, 1000, and 5000 with $u_0=0.1$ and $H=1.0$. The nonuniform mesh used is generated by the following transformation:

$$x=\frac{1}{2a}[a+\tanh(c\xi)], \quad y=\frac{1}{2a}[a+\tanh(c\eta)], \qquad (38)$$

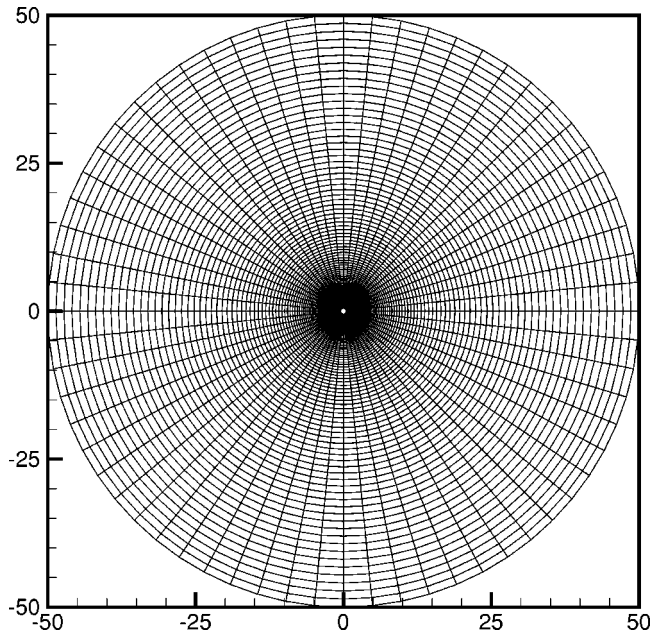

FIG. 10. Mesh distribution used for the flow over a circular cylinder.

where $a=\tanh(c)$ and $c=1.5$. The size of the mesh is $N_x \times N_y=64\times 64$. In all runs, the time step is set to be $\Delta t=0.1\times y_1$, where $y_1$ is the distance between the first fluid layer and the bottom plate. The parameter $\epsilon$ in the mixed scheme takes 0.1 for Re=400 and 1000, and 0.05 for Re =3200 and 5000 in order to decrease the numerical dissipation of the scheme. The streamlines of the flow for each case are plotted in Fig. 8. One can observe that the flow structures are in good agreement with the benchmark results proposed by Ghia *et al.* [29]. These plots show clearly the effect of the Reynolds number on the flow pattern. For flows with $\mathrm{Re}\leqslant 1000$, only three vortexes appear in the cavity: a primary one near the center and a pair of secondary ones in the lower corners of the cavity. At Re=3200, a third secondary vortex is seen in the upper left corner. As Re reaches 5000, a tertiary vortex appears in the lower right corner. It is also seen that the center of the primary vortex moves towards the center of the cavity as Re increases.

The two velocity components $u$ and $v$ along the vertical and horizontal lines through the cavity center are shown in Fig. 9 together with the benchmark solutions proposed by Ghia *et al.* [29]. Good agreements between the FDLBE solutions and the benchmark solutions are observed. The profiles become nearly linear in the center core of the cavity as Re increases. These observations are in agreement with the previous studies based on both traditional methods [29–31] and lattice Boltzmann methods with underlying uniform [32] or nonuniform lattice [21]. It is noted that, even when using a mesh of relatively small size ($64\times 64$) for $\mathrm{Re}\geqslant 3200$, the present FDLBE is able to capture the critical points. This is due to the nonuniform distribution of the mesh near the walls.

### E. The flow around a circular cylinder

Although the flow in a square cavity is complex, the geometry is nevertheless simple since only flat boundaries are

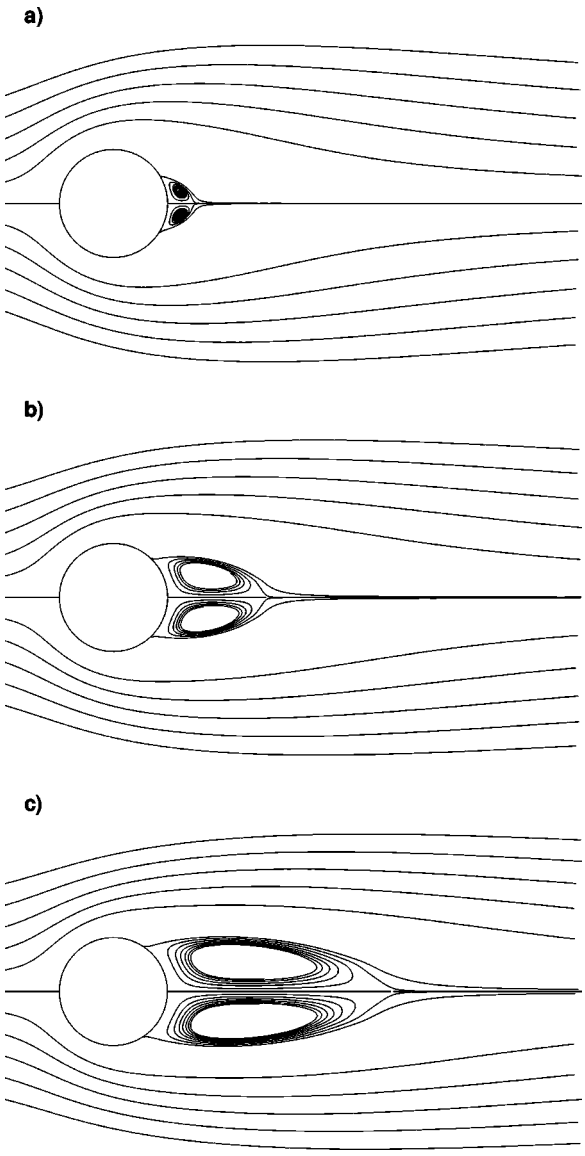


FIG. 11. Streamlines of the flow over a circular cylinder at different Reynolds numbers. (a) Re=10; (b) Re=20; and (c) Re =40.

involved. To demonstrate the capability of the present FDLBE, we apply it to the two-dimensional flow past a circular cylinder at different Reynolds numbers (10, 20, and 40) that are defined by $\mathrm{Re}=Du_0/\nu$, where $u_0$ is the free stream velocity and $D$ is the diameter of the cylinder.

The mesh employed in the calculation is generated in the usual polar coordinates $r$ and $\zeta$, where the $r$ direction is stretched by the following transformation similar to Eq. (32):

$$r_j = r_1 + (r_1 - r_0)\frac{\tanh(c\,\eta_j)}{\tanh c}, \tag{39}$$

where $r_0$ is the radius of the cylinder and $r_1$ is the outer boundary radius. $\eta_j = j/N_r - 1.0$ for $j=0,1,\ldots,N_r$, and $N_r$ is the number of grids in the $r$ direction. In our calculations, we take $r_0=0.5$, $r_1=50$, and c=3.5. The number of grid points in the $r$ and $\zeta$ directions are 129 and 64, respectively. The mesh setup is displayed in Fig. 10.

In simulations, the time step is set to be 0.1 times the minimum grid spacing. After a number of iterations, the flow reaches its steady state for each case. Figure 11 shows the streamlines of the flow at the final steady state. It is observed that a pair of stationary recirculating eddies appear behind the cylinder at the three Reynolds numbers considered. The wake length $L$, the distance from the rearmost point of the cylinder to the end of the wake, and the separation angle $\theta_s$ are measured and listed in Table I, together with related previous computational and experimental data. Both the wake length and separation angle agree well with the results of previous studies for the three Reynolds numbers considered. The dynamical parameters, the drag coefficient ($C_D$) and the stagnation pressure coefficients at the front $[C_p(\pi)]$ and at the end $[C_p(0)]$ of the cylinder are also measured as the flow reaches its steady state. As shown in Table II, these dynamical parameters agree well with the results of previous studies.

TABLE I. Comparision of geometrical parameters of the flow over a circular cylinder.

| | Re=10 | | Re=20 | | Re=40 | |
|---|---|---|---|---|---|---|
| | $L/r_0$ | $\theta_s$ | $L/r_0$ | $\theta_s$ | $L/r_0$ | $\theta_s$ |
| Ref. [33] | 0.434 | 27.96 | 1.786 | 43.37 | 4.357 | 53.34 |
| Ref. [34] | 0.68 | 32.5 | 1.86 | 44.8 | 4.26 | 53.5 |
| Ref. [5] | 0.474 | 26.89 | 1.842 | 42.9 | 4.490 | 52.84 |
| Ref. [12] | 0.498 | 30.0 | 1.804 | 42.1 | 4.38 | 50.12 |
| Present | 0.486 | 28.13 | 1.824 | 43.59 | 4.168 | 53.44 |

## IV. SUMMARY

In this paper, we have presented an explicit finite-difference-based lattice Boltzmann method. The starting point is the continuous Boltzmann equation for discrete velocities. As in the FDLBE proposed by Mei and Shyy [12],

TABLE II. Comparision of dynamical parameters of the flow over a circular cylinder.

| | Re=10 | | | Re=20 | | | Re=40 | | |
|---|---|---|---|---|---|---|---|---|---|
| | $C_D$ | $C_p(0)$ | $C_p(\pi)$ | $C_D$ | $C_p(0)$ | $C_p(\pi)$ | $C_D$ | $C_p(0)$ | $C_p(\pi)$ |
| Ref. [33] | 2.828 | −0.692 | 1.500 | 2.053 | −0.582 | 1.274 | 1.550 | −0.554 | 1.117 |
| Ref. [5] | 3.170 | −0.687 | 1.393 | 2.152 | −0.567 | 1.233 | 1.499 | −0.487 | 1.133 |
| Present | 3.049 | −0.661 | 1.467 | 2.048 | −0.512 | 1.289 | 1.475 | −0.448 | 1.168 |

the collision term is treated implicitly. However, the implicitness is completely cancelled by introducing a different distribution function, which results in an equivalent explicit scheme. Numerical simulations for several test problems have been conducted to validate the scheme. The numerical results confirm the reliability of the present FDLBE. It is noted that the same procedure can also be applied to other (e.g., finite-volume and finite-element) methods for discretization of the Boltzmann equation to form effective explicit lattice Boltzmann methods with nonuniform underlying lattices.

## ACKNOWLEDGMENT

The work described in this paper was fully supported by a grant from the Research Grants Council of the Hong Kong Special Administrative Region, China (Project No. HKUST6193/01E).

[1] R. Benzi, S. Succi, and M. Vergassola, Phys. Rep. **222**, 145 (1992).
[2] Y. Qian, S. Succi, and S.A. Orszag, Annu. Rev. Comput. Phys. **3**, 195 (1995).
[3] S. Chen and G. Doolen, Annu. Rev. Fluid Mech. **30**, 329 (1998).
[4] L-S. Luo, in Proceedings of Applied Comput. Fluid Dynamics., Beijing, 2000, edited by J-H. Wu (unpublished), pp. 52-83.
[5] X. He and L-S. Luo, Phys. Rev. E **55**, R6333 (1997).
[6] T. Abe, J. Comput. Phys. **131**, 241 (1997).
[7] X. He, S. Chen, and G.D. Doolen, J. Comput. Phys. **146**, 282 (1998).
[8] L-S. Luo, Phys. Rev. Lett. **81**, 1618 (1998).
[9] L-S. Luo and S.S. Girimaji, Phys. Rev. E **66**, 035301(R) (2002).
[10] M.B. Reider and J.D. Sterling, Comput. Fluids **24**, 459 (1995).
[11] N. Cao, S. Chen, S. Jin, and D. Martinez, Phys. Rev. E **55**, R21 (1997).
[12] R. Mei and W. Shyy, J. Comput. Phys. **143**, 426 (1998).
[13] J. Tölke *et al.*, Int. J. Mod. Phys. C **9**, 1143 (1998).
[14] G. Házi, Int. J. Mod. Phys. C **13**, 67 (1998).
[15] T. Seta and R. Takahashi, J. Stat. Phys. **107**, 557 (2002).
[16] F. Nannelli and S. Succi, J. Stat. Phys. **68**, 401 (1992).
[17] H. Chen, Phys. Rev. E **58**, 3955 (1998).
[18] G. Peng, H. Xi, C. Duncan, and S-H. Chou, Phys. Rev. E **58**, R4124 (1998).
[19] G. Peng, H. Xi, C. Duncan, and S-H. Chou, Phys. Rev. E **59**, 4675 (1999).
[20] H. Xi, G. Peng, and S-H. Chou, Phys. Rev. E **59**, 6202 (1999).
[21] T. Lee and C-L. Lin, J. Comput. Phys. **171**, 336 (2001).
[22] Y. Qian, D. d'Humiéres, and P. Lallemand, Europhys. Lett. **17**, 479 (1992).
[23] J.D. Sterling and S. Chen, J. Comput. Phys. **123**, 196 (1996).
[24] P.A. Skordos, Phys. Rev. E **48**, 4823 (1993).
[25] S. Chen, D. Martinez, and R. Mei, Phys. Fluids **8**, 2527 (1996).
[26] Q. Zou and X. He, Phys. Fluids **9**, 1591 (1997).
[27] Z.L. Guo, C.G. Zheng, and B.C. Shi, Chin. Phys. **11**, 366 (2002).
[28] Z.L. Guo, C.G. Zheng, and B.C. Shi, Phys. Fluids **14**, 2007 (2002).
[29] U. Ghia, K.N. Ghia, and C.T. Shin, J. Comput. Phys. **48**, 387 (1982).
[30] R. Schreiber and H. Keller, J. Comput. Phys. **49**, 310 (1983).
[31] S.P. Vanka, J. Comput. Phys. **65**, 138 (1986).
[32] S. Hou and Q. Zou, J. Comput. Phys. **118**, 329 (1995).
[33] F. Nieuwstadt and H.B. Keller, Comput. Fluids **1**, 59 (1973).
[34] M. Coutanceau and R. Bouard, J. Fluid Mech. **79**, 231 (1977).